Journal of Materials Chemistry A

Aluminum Enhances Photochemical Charge Separation in Strontium Titanate Nanocrystal Photocatalysts for Overall Water Splitting

Journal:	*Journal of Materials Chemistry A*
Manuscript ID	TA-ART-06-2018-005885.R1
Article Type:	Paper
Date Submitted by the Author:	31-Jul-2018

Complete List of Authors:	Zhao, Zeqiong; University of California, Department of Chemistry Willard, Emma; UC Davis Li, Hui; UC Davis Wu, Zongkai; UC Davis Castro, Ricardo; University of California at Davis, Chemical Engineering and Materials Science Osterloh, Frank ; University of California, Department of Chemistry

Aluminum Enhances Photochemical Charge Separation in Strontium Titanate Nanocrystal Photocatalysts for Overall Water Splitting

Zeqiong Zhao,[†] Emma J. Willard,[†] Hui Li,[‡] Zongkai Wu,[†] Ricardo H. R. Castro,[‡] Frank E. Osterloh[†]*

[†]Department of Chemistry, University of California Davis, One Shields Avenue, Davis, California 95616, United States and [‡]Department of Materials Science and Engineering, University of California Davis, One Shields Avenue, Davis, California 95616, United States

KEYWORDS: Al:$SrTiO_3$ · nanocrystals · overall water splitting · surface photovoltage spectroscopy · photosynthesis

ABSTRACT

Strontium titanate ($SrTiO_3$) is a well-known photocatalyst for overall water splitting (OWS) under ultra-violet irradiation. Recently, it was shown that Al-doped $SrTiO_3$ microparticles prepared by flux-mediated solid-state reaction catalyze OWS with an apparent quantum efficiency of 30% at 360 nm, the highest value reported so far for strontium titanate. However, the roles of Al^{3+} and of the particle morphology in controlling the activity are not clear. Here we report a new synthetic route to well defined nanocrystals of Al:$SrTiO_3$ with controllable Al-concentration (3-8 atom%) using TiO_2, $Sr(OH)_2$ and $Al(NO_3)_3$ as starting materials. X-ray diffraction and transmission electron microscopy confirm the presence of perovskite-type cubic nanoparticles with size of 60 nm. After loading with a $Rh_{2-y}Cr_yO_3$ cocatalyst, nano-Al:$SrTiO_3$ catalyzes OWS under UV/vis illumination from a Xe lamp. The activity shows a volcano-like dependence on Al concentration, confirming that Al^{3+} content is a key factor for the activity. Nanocrystals doped with 7.2 atom% Al show the activity of 53 μmol H_2 per hour under 240 $mW \cdot cm^{-2}$ UV illumination and an AQE of 0.06% at 375 nm. Based on surface photovoltage spectroscopy (SPS), aluminum enhances photochemical charge separation in the Al:$SrTiO_3$ nanocrystals and reduces electron trapping on Ti^{3+} sites. However, the Al:$SrTiO_3$ nanocrystals are found to be 20 times less active than Al:$SrTiO_3$ microparticles made by flux reaction in $SrCl_2$. The lower activity of the nanoparticles is due to optical shielding from the $Rh_{2-y}Cr_yO_3$ co-catalyst.

INTRODUCTION

Overall water splitting (OWS) with suspended semiconductor photocatalysts is one of the most promising options for carbon-free generation of hydrogen fuel from water and solar energy. [1-3] Over the years, various materials for OWS have been reported, but many suffer from low stability.[4-14] Metal oxide absorbers (La-doped $NaTaO_3$, [15] E_G = 4.1 eV and Zn-doped Ga_2O_3, E_G = 4.4 eV) are more stable but require high energy photons for operation (>4.0 eV). [16-18] Among metal oxides, $SrTiO_3$ (E_G = 3.2 eV) stands out because it can drive OWS under 3.2 eV illumination. [19-26] More recently it was shown that doping of $SrTiO_3$ with group 1, 2 and 13 elements (M = Li^+, Na^+, K^+, Rb^+, Cs^+, Mg^{2+}, Al^{3+}, Ga^{3+}, and In^{3+}) greatly enhances OWS activity.[27-30] For example, aluminum doped $SrTiO_3$ obtained by flux-synthesis in $SrCl_2$, in combination with a $Rh_{2-y}Cr_yO_3$ co-catalyst, supports OWS at AQY of 30% at 360 nm. [31, 32] The high activity was attributed to a reduction of the surface defects in the well-formed cubic microcrystals and to a reduction of Ti^{3+} lattice defects from Al^{3+} incorporation. [29, 30] In an attempt to develop additional synthetic avenues to this important photocatalyst and to promote the understanding of the effects of morphology and Al doping on activity, we report here a novel hydrothermal synthesis of Al:$SrTiO_3$ nanocrystals with controllable Al doping amount (0-8 atom%) and constant particle size. The OWS activity of Al:$SrTiO_3$ shows a volcano-type dependence on the amount of aluminum dopant, with an optimum achieved at 7.2 atom%. The OWS activity is also correlated with the photovoltage size and photovoltage reversibility of the samples, as measured by surface photovoltage spectroscopy (SPS). This suggests that Al improves photochemical charge separation in Al:$SrTiO_3$ nanocrystals and that it reduces the degree of electron trapping. This explains the higher activity of the material in comparison with non-doped $SrTiO_3$. However, the activity of Al:$SrTiO_3$ nanocrystals is also found to be ~20 times

lower than that of Al:$SrTiO_3$ *microparticles* prepared by the known flux synthesis. Reference H_2 evolution experiments show that this activity loss can be attributed to increased optical shielding from the co-catalyst.

RESULTS AND DISCUSSION

Al:$SrTiO_3$ nanoparticles were obtained by heating a mixture of solid $Sr(OH)_2$, TiO_2, $Al(NO_3)_3$, and KOH in water to 150 ^oC in an autoclave for 72 h.[23] After cooling to room temperature, and washing the precipitate with water and mild hydrochloric acid to remove starting materials, the product is obtained as an off-white solid. Al:$SrTiO_3$ nanoparticles with 3-8 atom% incorporated Al dopant can be successfully synthesized in this way by varying the $Al(NO_3)_3$ amount between 10 – 90 atom% (based on $Sr(OH)_2$). Powder X-ray diffraction (PXRD) patterns for pure $SrTiO_3$ and Al:$SrTiO_3$ nanocrystals obtained from hydrothermal method are shown in **Figure 1** and **Figure S1.** They confirm the perovskite crystal structure of $SrTiO_3$ (JPDF #35-0734). As shown in the inset in **Figure 1**, the diffraction peaks of Al:$SrTiO_3$ nanoparticles shifted to a higher angle compared to pure $SrTiO_3$ nanoparticles. Based on Bragg's law, the unit cell of 7.2 atom% Al:$SrTiO_3$ is 0.2% smaller than the unit cell of pure $SrTiO_3$, indicating successful incorporation of Al atoms in Ti sites in $SrTiO_3$ nanocrystals.

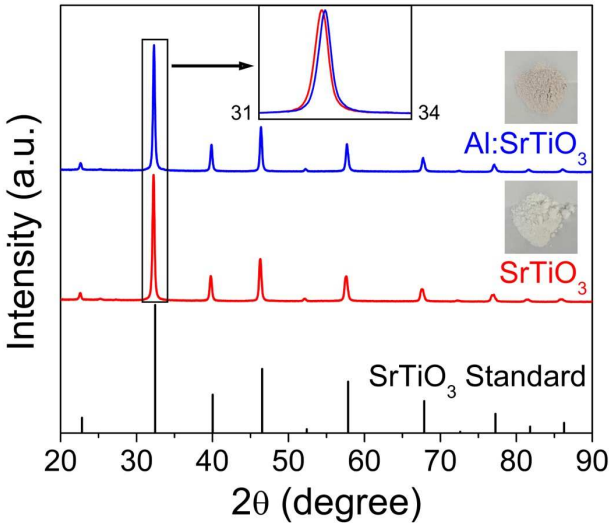

Figure 1 PXRD patterns of nano-$SrTiO_3$ and 7.2 atom% nano-Al:$SrTiO_3$ with reference pattern for $SrTiO_3$ (JPDF #35-0734) at the bottom and photos as inserts. The main diffraction peak is magnified to illustrate the shift from 31° to 34° for nano-Al:$SrTiO_3$. The small peak at 25.3° corresponds to unreacted TiO_2 starting material.

Transmission electron microscope (TEM) images in **Figures 2** show that Al:$SrTiO_3$ nanocrystals have a cubic or spherical shape and average sizes of 60 nm (see also **Table 1**). The shape and size of the nanocrystals is independent of the amount of added $Al(NO_3)_3$ (**Figure S2**).

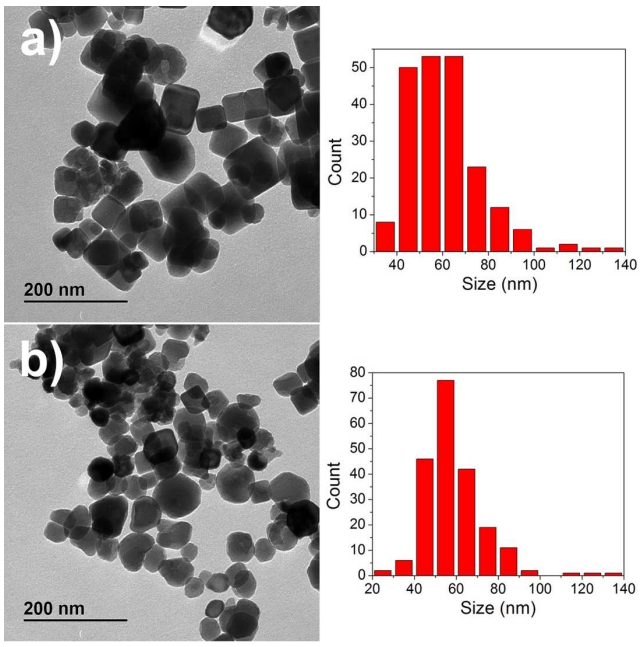

Figure 2 TEM images and size histograms of (a) nano-$SrTiO_3$, (b) nano-Al:$SrTiO_3$ with 7.2 atom% aluminum.

Table 1 Size analysis and Al amounts of nano-Al:$SrTiO_3$. Additional data in **Figure S2** and **Table S1.**

Al Precursor Amount	Average Size (nm)	Al Dopant Amount in atom% 2[Al] / ([Sr]+[Ti]+[Al]) * 100%
0% Al	61.0 ± 16.6	-
10% Al	60.4 ± 11.8	3.2 %
20% Al	60.2 ± 11.7	4.5 %
30% Al	57.1 ± 11.9	4.8 %
50% Al	59.7 ± 14.6	6.1 %
70% Al	59.5 ± 17.5	7.2 %
90% Al	59.0 ± 13.0	7.8 %

The Al dopant amount in nano-Al:$SrTiO_3$ (**Table 1**) was determined with X-ray Fluorescence (XRF). Aluminum concentrations vary from 3.2 to 7.8 atom% depending on the amount of

$Al(NO_3)_3$ present during the synthesis. That means that only a small fraction of Al^{3+} is incorporated into the product.

To achieve OWS with Al:$SrTiO_3$, a $Rh_{2-y}Cr_yO_3$ selective proton reduction co-catalyst is also required. [31-34] To find the optimum co-catalyst loading ratio, variable amounts of $Rh_{2-y}Cr_yO_3$ were deposited onto 7.2 atom% nano-Al:$SrTiO_3$ via the published impregnation/calcination route. [31, 32] The OWS performance of the resulting composites was evaluated in pure water under full Xe spectrum illumination (**Figure S3**). At low loadings (0.5 wt% Rh) only sub-stoichiometric amounts of hydrogen and oxygen were produced, but a 2:1 ratio was obtained at 1.0-2.0 wt% Rh, with 1.0 wt% of Rh yielding higher activity. Next, in order to identify the optimum Al^{3+} concentration in the nanocrystals, OWS was performed with all $Rh_{2-y}Cr_yO_3$/Al:$SrTiO_3$ catalysts. The results are shown in **Figure 3(a)**, **3(b)** and **Figure S4**. It can be seen that nano-$SrTiO_3$ without Al produced only small amounts of H_2 and no detectable O_2. Samples with 3.2 atom% Al produced H_2/O_2 in 1.41:1 molar ratio. Stoichiometric water splitting was achieved with 4.5 atom% or greater Al content, and the highest activity of 53 μmol H_2 per hour was found for 7.2 atom% Al. When the Al concentration was increased to 7.8 atom%, the activity drops to 36 μmol/h. This is a possible result of lattice defects connected to Al incorporation. Overall, OWS with nano-Al:$SrTiO_3$ shows a volcano-type dependence on the amount of aluminum dopant. This confirms Al^{3+} content as a key factor for OWS.

Further insight into the specific function of the Al dopants was sought by observing the optical and photophysical properties of the samples. On the basis of the optical absorption spectra in **Figure 4(a)** and **Figure S5**, the bandgap for nano-$SrTiO_3$ is 3.2 eV (yellow region), which is in agreement with previous reported value.[35] Samples of nano-Al:$SrTiO_3$ have the same absorption onset, but additionally contains a weak absorption feature in the 1.7-3.0 eV region that increases

with Al content (**Figure S5)**. Tentatively, we attribute this feature to excitation of oxygen vacancies in the lattice. Such oxygen vacancies can be introduced by the doping of a cation (Al^{3+}) with a valence lower than that of its parent cation (Ti^{4+}). [29]

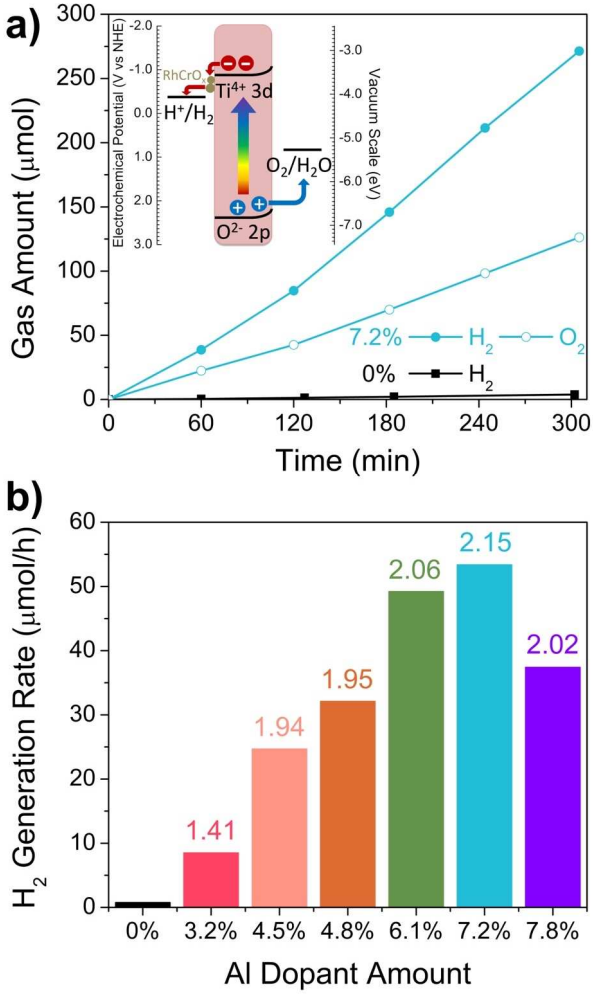

Figure 3 (a) Irradiation results of 1 wt% Rh, 1.5 wt% Cr, $Rh_{2-y}Cr_yO_3$ loaded nano-$SrTiO_3$ and 7.2 atom% nano-Al:$SrTiO_3$ in pure water under full spectrum of Xe lamp irradiation (240 mW/cm^2). Dots: H_2; circles: O_2. Inset: Energy diagram for OWS. (b) H_2 generation rate of 1wt% Rh, 1.5 wt% Cr, $Rh_{2-y}Cr_yO_3$ loaded nano-Al:$SrTiO_3$ versus Al concentration. Numbers shown above each bar indicate the H_2 to O_2 ratio. The measurement error (standard deviation) is 15 and

18% for H_2 and O_2 rates based on repeat measurements of several samples. Using a similar method, the error for the Al concentration was determined as 4%.

In order to probe photochemical charge separation in the catalysts, surface photovoltage spectra (SPS) of annealed nano-$SrTiO_3$ and nano-Al:$SrTiO_3$ particle films on FTO were recorded under a vacuum atmosphere using the vibrating Kelvin probe method. [36-38] Such spectra provide information about majority carrier type, intermediate states, and the effective band gap of the semiconductor.[36, 37, 39, 40] Selected spectra are shown in **Figure 4(a)** and a full set of SPS data for all Al-doped $SrTiO_3$ is presented in **Figure S6**. All samples produce a negative photovoltage indicative of majority carrier (electron) diffusion from the illuminated catalyst into the FTO support. For nano-$SrTiO_3$ the negative photovoltage is already observed starting at 1.8 eV. This suggests the presence of defects approximately 1.4 eV below the conduction band, which might be attributed to Ti^{3+} states (1.5–1.6 eV below CBM) and to oxygen-vacancy defects (1.9-2.6 eV below CBM) based on cathodoluminescence spectra of $SrTiO_3$.[41] The photovoltage gradually increases to -0.8 V at 2.5 eV, and then reaches its maximum value of -1.5 V at 3.4 eV, slightly above the band gap of the material. Above 3.5 eV the photovoltage decreases because the light output from the Xe lamp falls to zero and because of the diminishing light penetration depth of the sample. At the end of the scan, -0.8 V photovoltage remains, which corresponds to 50% of the photovoltage maximum. This indicates that 50% of the holes are trapped in nano-$SrTiO_3$, likely on Ti^{3+} sites originally present in the sample. The incorporation of Al leads to several changes in the photovoltage spectra of nano-Al:$SrTiO_3$ (**Figure 4(a)** and **S6**). First, the sub-gap signal is markedly reduced in the region below 2.5 eV, which indicates a reduction of mid-bandgap Ti^{3+} states. Second, the maximum photovoltage is increased to -3.4 V, which suggests

the presence of fewer recombination sites or better charge transport. Third, the residual photovoltage at the end of the scan is -0.9 V (26% of the maximum at 3.5 eV) which shows better reversibility of charge separation and fewer hole traps. These observations are in line with the results of Takata et al. that incorporation of a lower valence ion (Al^{3+}) inhibits the formation of Ti^{3+} defects. [29] Based on transient absorption spectroscopy Ti^{3+} states are also correlated with diminished carrier lifetimes and reduced OWS performance in $SrTiO_3$. [30] The SPS results support these interpretations.

In order to understand the photovoltage size, the energy diagram of the Al:$SrTiO_3$/FTO configuration must be considered (inset in **Figure 4(a)**). Based on earlier SPS measurements on Rh:$SrTiO_3$, [23] and Ru/Rh:$SrTiO_3$/$BiVO_4$ tandem photocatalysts, [42] two separate processes can contribute to the photovoltage. One is electron injection from the Al:$SrTiO_3$ conduction band to the Fermi level of FTO substrate and the other one is hole injection from valence band of Al:$SrTiO_3$ to surface states (H_2O, hydroxyl group, or surface Ti^{3+}). Based on these contributions (-1.6 V and -1.4 V), the maximum possible photovoltage for the FTO/Al:$SrTiO_3$ configuration is –3.0 V. The larger experimental value of -3.4 V suggests the presence of additional hole traps at more reducing potentials than water (+0.82 V at pH = 7). Interestingly, a plot of the maximum photovoltage versus Al concentration shows the same volcano-like dependence (**Figure 4(b)**) as the photocatalytic activity. That confirms that OWS activity and photovoltage generation in nano-Al:$SrTiO_3$ are correlated with each other. It provides further support for the earlier hypothesis that Al^{3+} reduces Ti^{3+} defects in Al:$SrTiO_3$ and improves electron-hole lifetimes.

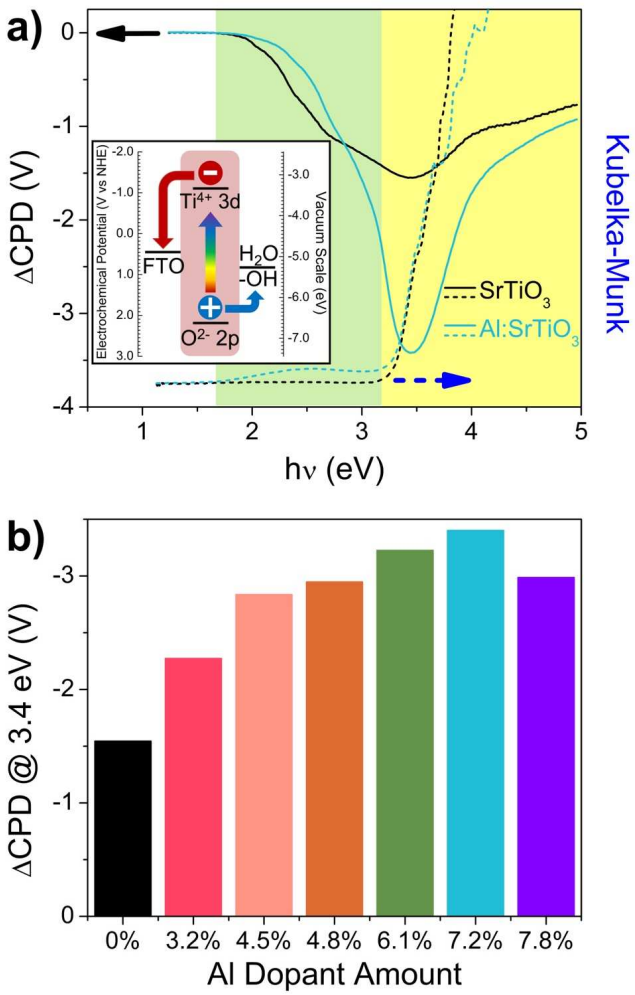

Figure 4 (a) UV-Vis diffuse reflectance spectra and surface photovoltage spectra of nano-$SrTiO_3$ and 7.2 atom% nano-Al:$SrTiO_3$. Inset is energy diagram for charge transfer process during SPS measurement (see also Wang et al. [23]). (b) Maximum photovoltage versus Al dopant concentration. The measurement error (standard deviation) of the photovoltage is 6% based on repeat measurements of several samples.

Lastly, in order to determine the effect of the particle morphology on OWS, we compare the photocatalytic activities of nano-Al:$SrTiO_3$ with that of Al:$SrTiO_3$ microparticles synthesized by

the known flux-reaction. [31] To synthesize the latter, a $SrTiO_3$ precursor was first obtained by solid state reaction of $SrCO_3$ and TiO_2 at 1000 °C for 10 h (denoted as ss-$SrTiO_3$),[43] and aluminum was then introduced into the lattice by heating the $SrTiO_3$ in a $SrCl_2$ flux inside of an aluminum crucible to 1100 °C for 10 h.[31] Selected data for the ss-$SrTiO_3$ intermediate and the micro-Al:$SrTiO_3$ product are summarized in **Figure 5**. According to scanning electron microscopy (SEM), micro-Al:$SrTiO_3$ forms cubic crystals with an average edge length of 343.4 nm, i.e. six times the value of the nanocrystals. Based on XRF and microprobe measurements, the Al^{3+} concentration in micro-Al:$SrTiO_3$ is between 1.2 and 2.1%. This exceeds the previously reported value of 0.3 % for a similar preparation.[31]

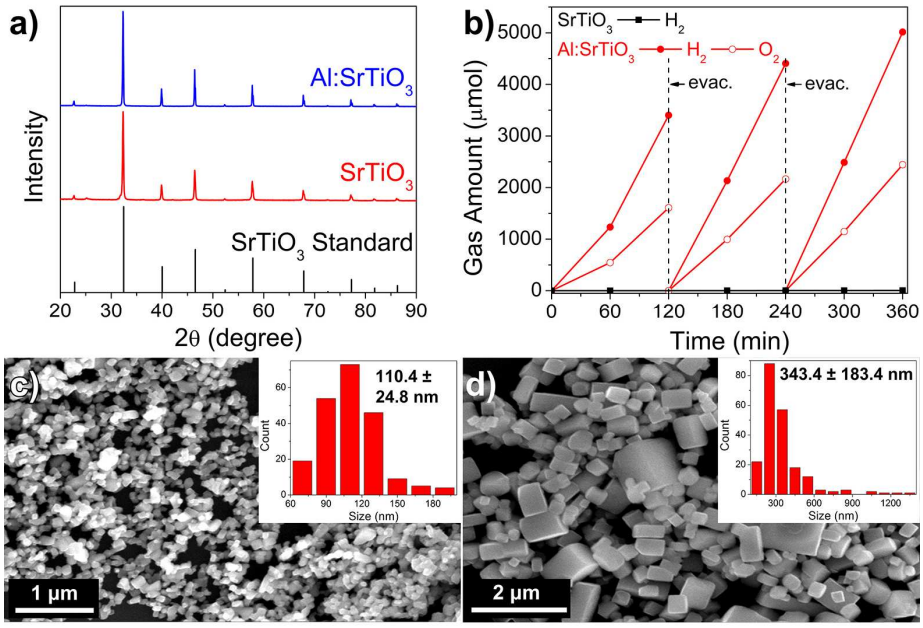

Figure 5 (a) PXRD patterns of ss-$SrTiO_3$ obtained from solid state reaction and micro-Al:$SrTiO_3$ from flux synthesis. (b) H_2/O_2 evolution from 0.17 wt% Rh, 0.26 wt% Cr, $Rh_{2-y}Cr_yO_3$ loaded ss-$SrTiO_3$ and micro-Al:$SrTiO_3$ in pure water under full spectrum Xe irradiation (320 mW/cm^2 by UV detector). Evacuations were performed to keep H_2/O_2 pressure below the explosive limit.

SEM images and size histograms of (c) ss-$SrTiO_3$ nanoparticles from solid state reaction and (d) micro-Al:$SrTiO_3$ from flux-synthesis.

To prepare for the OWS experiment, micro-Al:$SrTiO_3$ and ss-$SrTiO_3$ were loaded with Cr, $Rh_{2-y}Cr_yO_3$ co-catalyst using the same procedure as for the nanomaterial. The loading amount (0.17 wt% Rh and 0.26 wt%) on micro-Al:$SrTiO_3$ was chosen to achieve the same coverage per surface area as for the $Rh_{2-y}Cr_yO_3$ loaded 7.2 atom% nano-Al:$SrTiO_3$. Details of the surface area calculation are given in the supporting information. As shown in **Figure 5(b)**, cocatalyst modified ss-$SrTiO_3$ produces 1 μmol H_2 per hour, whereas micro-Al:$SrTiO_3$ produces 2.3 mmol H_2 per hour with stoichiometric amounts of O_2. This activity is ~40 times greater than for the nanocrystals. Under monochromatic illumination from a 375 nm LED, the 0.17 wt% Rh, 0.26 wt% Cr, $Rh_{2-y}Cr_yO_3$ loaded micro-Al:$SrTiO_3$ has an apparent quantum yield (AQY) of 16.1%. In comparison, the 1 wt% Rh, 1.5 wt% Cr, $Rh_{2-y}Cr_yO_3$ modified 7.2 atom% nano-Al:$SrTiO_3$ only has an AQY of 0.06%, a factor of over 260 difference. We hypothesize that the 40-260 activity difference is partially due to optical shading from the $Rh_{2-y}Cr_yO_3$ cocatalyst. Because nano-Al:$SrTiO_3$ requires six times the amount of $Rh_{2-y}Cr_yO_3$ to reach its optimum performance, competitive light absorption from the cocatalyst is also six times stronger. Indeed, the $Rh_{2-y}Cr_yO_3$ cocatalyst absorbs light strongly between 1.6 eV and the band edge of Al:$SrTiO_3$ (**Fig. 6(a)**). Shading from this feature particularly significant under 3.3 eV illumination, because of the relatively low absorption of Al:$SrTiO_3$ at this energy. To further test the shading hypothesis, micro-Al:$SrTiO_3$ were prepared at a cocatalyst loading (1 wt% Rh and 1.5 wt% Cr) equal to that of the most active nano-Al (7.2%):$SrTiO_3$ / $Rh_yCr_{2-y}O_3$ catalyst. As shown in **Figure 6(b)**, the higher cocatalyst loading reduces the OWS activity of micro-Al:$SrTiO_3$ catalyst 20 times, so that

at equal loading, micro- and nano-Al:$SrTiO_3$ now only differ by a factor of two in activity. This suggests that the co-catalyst shading effect as the main cause for the lower OWS activity of nano-Al:$SrTiO_3$. The remaining activity difference may be attributed to other effects, incl. interference of the cocatalyst with hole transfer across the solid-liquid junction at the Al:$SrTiO_3$-liquid interface. [44]

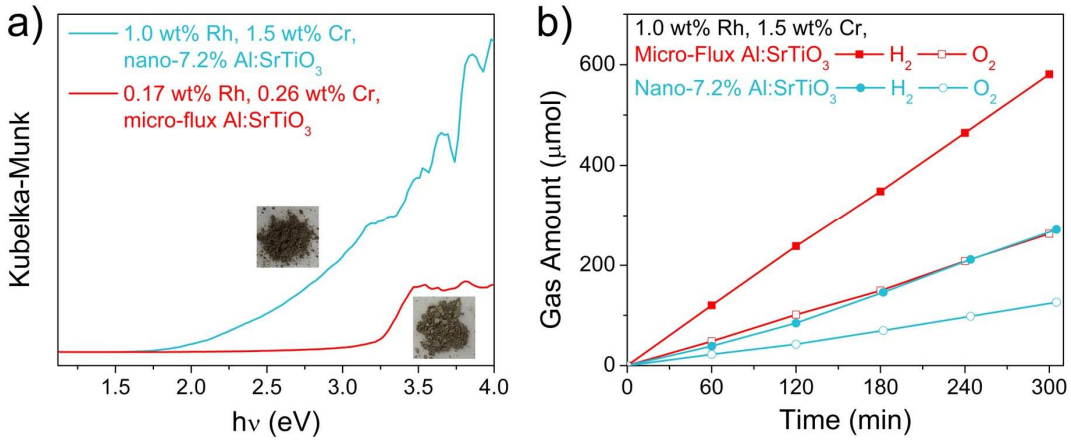

Figure 6 a) UV-Vis diffuse reflectance spectra and photos of 1 wt% Rh, 1.5 wt% Cr, $Rh_{2-y}Cr_yO_3$ loaded 7.2% nano-Al:$SrTiO_3$ and 0.17 wt% Rh, 0.26 wt% Cr, $Rh_{2-y}Cr_yO_3$ loaded micro-Al:$SrTiO_3$. b) H_2 evolution from 1.0 wt% Rh, 1.5 wt% Cr, $Rh_{2-y}Cr_yO_3$ loaded micro-Al:$SrTiO_3$ and 1.0 wt% Rh, 1.5 wt% Cr, $Rh_{2-y}Cr_yO_3$ loaded nano-Al(7.2%):$SrTiO_3$ nanoparticles in pure water under full spectrum of Xe lamp irradiation.

CONCLUSIONS

Cubic Al:$SrTiO_3$ nanocrystals of perovskite-type structure and with controllable Al^{3+} concentration were synthesized for the first time. After modification with a $Rh_yCr_{2-y}O_3$ cocatalyst, the nanocrystals were active for overall water splitting under full spectrum Xe lamp

illumination. The photocatalytic activity showed a volcano-like dependence with regard to the amount of aluminum dopant. At the optimal Al concentration and co-catalyst amount, the apparent quantum efficiency was 0.06% at 375 nm. The photocatalytic activity correlates with the photovoltage of the nanocrystals, as measured by SPS and is inversely related to the residual photovoltage after illumination. This suggests that incorporation of Al^{3+} into the lattice reduces the concentration of Ti^{3+} sub-bandgap defects that cause recombination and charge trapping, in support of an earlier interpretation on the basis of transient IR absorption measurements.[30] Compared to Al:$SrTiO_3$ microcrystals, the Al:$SrTiO_3$ nanocrystals are 20 times less active under UV/vis irradiation, and 260 times less active under 375 nm LED illumination. Reference experiments show that this difference is mostly due to optical shading effects from the $Rh_{2-y}Cr_yO_3$ cocatalyst. These results give insight into the factors that control energy conversion with suspended photocatalyst particles.

EXPERIMENTAL SECTION

Chemicals

Strontium hydroxide octahydrate (99%, Alfa Aesar), titanium (IV) oxide P25 (99.5%, Acros Organics), potassium hydroxide, (≥85%, Sigma-Aldrich), strontium chloride hexahydrate (99%, EM Science), aluminium nitrate nonahydrate (98.1%, Fisher Scientific), rhodium chloride, chromium (III) nitrate nonahydrate (99%, Acros Organics), hydrochloric acid (36.5-38.0%, EMD), alumina crucible (Fisher) were used as received. Water was purified to 18 MΩ·cm resistivity by a Nanopure system.

Syntheses

Hydrothermal (HT) Synthesis of Al:$SrTiO_3$: The synthesis was similar to the previously reported method for Rh-doped $SrTiO_3$. [23] Specified amounts of $Sr(OH)_2 \cdot 8H_2O$, P25 TiO_2 and $Al(NO_3)_3 \cdot 9H_2O$ (as shown in Table 2) were added to a Teflon lined autoclave, followed by 22.5 mmol KOH (1.2625 g) and then 23 mL of water. The suspension was mixed well by shaking and the autoclave was heated to 150 ^oC for 72 h. The autoclave was then cooled to room temperature, and the suspension was centrifuged and the off-white solid washed four times with water, three times with aqueous 0.1 $mol \cdot L^{-1}$ HCl solution and three more times with water. Finally, the suspension was centrifuged and the off-white solid was collected in 60-80% yield and dried under vacuum overnight.

Table 2 Reagents amounts for the synthesis of Al:$SrTiO_3$

	$Sr(OH)_2 \cdot 8H_2O$	TiO_2	$Al(NO_3)_3 \cdot 9H_2O$
$SrTiO_3$	0.5980 g	0.1795 g	0
$SrTiO_3$ with 10% Al^{3+}	0.5980 g	0.1618 g	0.0844 g
$SrTiO_3$ with 20% Al^{3+}	0.5980 g	0.1618 g	0.1684 g
$SrTiO_3$ with 30% Al^{3+}	0.5980 g	0.1618 g	0.2532 g
$SrTiO_3$ with 50% Al^{3+}	0.5980 g	0.1618 g	0.4220 g
$SrTiO_3$ with 70% Al^{3+}	0.5980 g	0.1618 g	0.5908 g
$SrTiO_3$ with 90% Al^{3+}	0.5980 g	0.1618 g	0.7596 g

Flux-mediated Synthesis of Al:$SrTiO_3$:[31, 43] 3.10 g of $SrCO_3$ was calcined in air at 300 ^oC for 1 h before use. 1.68 g TiO_2 and 3.10 g $SrCO_3$ were well mixed by wet grinding in ethanol. Afterwards, the mixture was heated to 1000 ^oC for 10 hours in a covered ceramic crucible to yield a white powder, designated as ss-$SrTiO_3$, in 95% yield. For the flux treatment, 0.37 g of the

solid was ground with 5.33 g $SrCl_2 \cdot 6H_2O$ (mole ratio of $SrCl_2/SrTiO_3$ =10) for 5 min and the mixture heated to 1100 ^oC in a covered alumina crucible. After 10 h, the crucible was cooled to room temperature and the off-white molten solid was washed with water until no white AgCl precipitate formed in the wash upon adding dilute aqueous $AgNO_3$ solution. Al:$SrTiO_3$ was obtained as an off-white solid in 90% overall yield.

Deposition of $Rh_{2-y}Cr_yO_3$ co-catalyst on Al:$SrTiO_3$: The cocatalyst was deposited by impregnation/calcination as previously reported by Maeda et al.[45] 150 mg Al:$SrTiO_3$ and 4 mL water containing 3.8 mg of $RhCl_3 \cdot xH_2O$ and 17.3 mg of $Cr(NO_3)_3 \cdot 9H_2O$ were placed in an open glass vial and heated to 80 ^oC in a water bath with occasional stirring. The resulting powder was collected after approximately 1 h and heated in air at 350 ^oC for 1 h to produce $Rh_{2-y}Cr_yO_3$ /Al:$SrTiO_3$ in 95% yield.

Characterization

Transmission electron microscopy (TEM) images were recorded using a Philips CM-120 at 80 kV. Sample suspension was dropped onto carbon coated Cu-grids and allowed to dry in air naturally. Scanning electron microscopy (SEM) images were recorded with a Philips XL-30 Scanning Electron Microscope using samples prepared on silicon wafers by drop coating followed by drying in air naturally. Powder X-ray diffraction scans were performed using a Bruker D8 Advance Eco with Cu Kα X-ray radiation (λ = 1.5418 Å). X-ray fluorescence spectroscopy (Rigaku, Supermini200 Sequential WD-XRF, Pd Target, 50kV, 4mA, Tokyo, Japan) and Cameca SX-100 electron microprobe were used to determine the Al dopant amount in $SrTiO_3$. UV/Vis diffuse reflectance spectra and absorption spectra were recorded on a Thermo

Scientific Evolution 220 UV Vis spectrometer equipped with an integrating sphere. The film thickness was measured by Dektak 150 profilometer after the SPS measurement. Surface photovoltage (SPS) measurements were conducted under vacuum (7×10^{-5} mBar) using a vibrating gold Kelvin probe (Delta PHI Besocke) as the reference electrode. Samples were illuminated with monochromatic light from a 150 W Xe lamp filtered through an Oriel Cornerstone 130 monochromator (0.1-0.3 mW cm^{-2}). SPS data was corrected for drift effects by subtracting a dark scan. Sample films were prepared via the following method. Fluorine-doped tin oxide (FTO) substrates were sonicated sequentially in methanol, acetone, and 2-propanol, rinsed with water, and dried under vacuum before use. Then, ~6 mg Al:$SrTiO_3$ was suspended in 1 mL water and sonicated for 3 h. Of the resulting suspension, 0.1 mL was drop-coated on a 0.8 $\times$ 0.8 cm^2 FTO substrate and allowed to dry in air. The films were then heated at 300 ^oC for 2 h before measurement.

Photocatalytic hydrogen and oxygen evolution tests were performed by placing 100 mg of each catalyst and 100 mL water inside of a 165 mL quartz glass flask. The suspension was sonicated for 15 min and degassed with N_2 for 20 min to remove the residual oxygen gas dissolved in the water. The flask was connected to an airtight gas sampling system and purged with argon until no more air could be detected in the head space. The gas flow was turned off and the suspension was evacuated to approximately 600 torr. The flask was then irradiated with an Xe lamp (light intensity was measured at the flask surface by an International Light IL1400BL photometer equipped with a SED (SEL) 365 detector for 230 to 380 nm sensitivity range) and gas samples were withdrawn periodically via the gas sampling system and analyzed with a Varian 3800 gas chromatograph equipped with a 60/80 Å molecular sieve column and thermal conductivity detector.

ASSOCIATED CONTENT

Supporting Information. X-ray diffraction pattern, TEM images, XRF data, H_2/O_2 evolution results, photovoltage spectra, and elemental analysis data.

AUTHOR INFORMATION

Corresponding Author

*fosterloh@ucdavis.edu

ACKNOWLEDGMENT

We thank Prof. Adam Moulé (UC Davis) for access to the profilometer and the National Science Foundation (grant CHE 1464938) for financial support of this work.

REFERENCES

1. M. G. Walter, E. L. Warren, J. R. McKone, S. W. Boettcher, Q. X. Mi, E. A. Santori and N. S. Lewis, *Chem. Rev.*, 2010, **110**, 6446-6473.
2. R. Krol, *Photoelectrochemical Hydrogen Production*, 2012, **102**, 13-67.
3. A. J. Bard and M. A. Fox, *Acc. Chem. Res.*, 1995, **28**, 141-145.
4. D. M. Fabian, S. Hu, N. Singh, F. A. Houle, T. Hisatomi, K. Domen, F. E. Osterloh and S. Ardo, *Energ. & Envi. Sci.*, 2015, **8**, 2825-2850.
5. F. E. Osterloh, *Chem. Soc. Rev.*, 2013, **42**, 2294-2320.
6. T. Hisatomi, J. Kubota and K. Domen, *Chem. Soc. Rev.*, 2014, **43**, 7520-7535.
7. K. Wu and T. Lian, *Chem. Soc. Rev.*, 2016, **45**, 3781-3810.
8. K. Sivula and R. van de Krol, *Nature Reviews Materials*, 2016, **1**, 15010.

9. S. J. A. Moniz, S. A. Shevlin, D. J. Martin, Z.-X. Guo and J. Tang, *Energ. & Environ. Sci.*, 2015, **8**, 731-759

10. R. Marschall, *Adv. Func. Mater.*, 2014, **24**, 2421-2440.

11. K. Maeda, *ACS Catalysis*, 2013, **3**, 1486-1503.

12. B. Mei, A. A. Permyakova, R. Frydendal, D. Bae, T. Pedersen, P. Malacrida, O. Hansen, I. E. L. Stephens, P. C. K. Vesborg, B. Seger and I. Chorkendorff, *J. Phys. Chem. Lett.*, 2014, **5**, 3456-3461.

13. A. Paracchino, V. Laporte, K. Sivula, M. Graetzel and E. Thimsen, *Nat. Mater.*, 2011, **10**, 456-461.

14. J. Boltersdorf, I. Sullivan, T. L. Shelton, Z. Wu, M. Gray, B. Zoellner, F. E. Osterloh and P. A. Maggard, *Chem. Mater.*, 2016, **28**, 8876-8889.

15. H. Kato, K. Asakura and A. Kudo, *J. Am. Chem. Soc.*, 2003, **125**, 3082-3089.

16. C. X. Kronawitter, L. Vayssieres, S. H. Shen, L. J. Guo, D. A. Wheeler, J. Z. Zhang, B. R. Antoun and S. S. Mao, *Energ. & Environ. Sci.*, 2011, **4**, 3889-3899.

17. A. Wolcott, W. A. Smith, T. R. Kuykendall, Y. P. Zhao and J. Z. Zhang, *Adv. Funct. Mater.*, 2009, **19**, 1849-1856.

18. Y. Sakata, T. Hayashi, R. Yasunaga, N. Yanaga and H. Imamura, *Chem. Commun.*, 2015, **51**, 12935-12938.

19. K. Domen, A. Kudo, T. Onishi, N. Kosugi and H. Kuroda, *J. Phys. Chem. C.*, 1986, **90**, 292-295.

20. K. Domen, S. Naito, M. Soma, T. Onishi and K. Tamaru, *J. Chem. Soc., Chem. Commun.*, 1980, 543-544.

21. T. K. Townsend, N. D. Browning and F. E. Osterloh, *ACS Nano*, 2012, **6**, 7420–7426.

22. T. K. Townsend, N. D. Browning and F. E. Osterloh, *Energ & Env. Sci.*, 2012, **5**, 9543-9550.

23. J. Wang, J. Zhao and F. E. Osterloh, *Energ. & Envi. Sci.*, 2015, **8**, 2970-2976.

24. L. Mu, Y. Zhao, A. Li, S. Wang, Z. Wang, J. Yang, Y. Wang, T. Liu, R. Chen, J. Zhu, F. Fan, R. Li and C. Li, *Energ. & Environ. Sci.*, 2016, **9**, 2463-2469.

25. A. Kumar, P. G. Santangelo and N. S. Lewis, *J. Phys. Chem.*, 1992, **96**, 834-842.

26. K. Han, T. Kreuger, B. Mei and G. Mul, *ACS Catalysis*, 2017, **7**, 1610-1614.

27. H. Kato, M. Kobayashi, M. Hara and M. Kakihana, *Catalysis Science & Technology*, 2013, **3**, 1733-1738.

28. Y. Sakata, Y. Miyoshi, T. Maeda, K. Ishikiriyama, Y. Yamazaki, H. Imamura, Y. Ham, T. Hisatomi, J. Kubota, A. Yamakata and K. Domen, *Applied Catalysis A: General*, 2016, **521**, 227-232.

29. T. Takata and K. Domen, *J. Phys. Chem. C*, 2009, **113**, 19386-19388.

30. A. Yamakata, H. Yeilin, M. Kawaguchi, T. Hisatomi, J. Kubota, Y. Sakata and K. Domen, *J. Photoch. Photobio. A*, 2015, **313**, 168-175.

31. Y. Ham, T. Hisatomi, Y. Goto, Y. Moriya, Y. Sakata, A. Yamakata, J. Kubota and K. Domen, *J. Mater. Chem. A*, 2016, **4**, 3027-3033.

32. Y. Ham, T. Minegishi, T. Hisatomi and K. Domen, *Chem. Commun.*, 2016, **52**, 5011-5014.

33. K. Maeda, K. Teramura, D. Lu, T. Takata, N. Saito, Y. Inoue and K. Domen, *Nature*, 2006, **440**, 295.

34. K. Maeda, K. Teramura, N. Saito, Y. Inoue and K. Domen, *Journal of Catalysis*, 2006, **243**, 303-308.

35. K. v. Benthem, C. Elsasser and R. H. French, *J. Appl. Phys.*, 2001, **90**, 6156-6164.

36. M. A. Melo, Jr., Z. Wu, B. A. Nail, A. T. De Denko, A. F. Nogueira and F. E. Osterloh, *Nano Lett*, 2018, **18**, 805-810.

37. J. Zhao, B. A. Nail, M. A. Holmes and F. E. Osterloh, *J Phys Chem Lett*, 2016, **7**, 3335-3340.

38. M. K. Nowotny, P. Bogdanoff, T. Dittrich, S. Fiechter, A. Fujishima and H. Tributsch, *Mater. Lett.*, 2010, **64**, 928-930.

39. X. Ma, X. Cui, Z. Zhao, M. A. Melo, E. J. Roberts and F. E. Osterloh, *Journal of Materials Chemistry A*, 2018, **6**, 5774-5781.

40. J. Wang, J. Zhao and F. E. Osterloh, *Energy Environ. Sci.*, 2015, **8**, 2970-2976.

41. R. A. Rosenberg, Y. Choi, K. Vijayalakshmi, M. Kareev, J. Tchakhalian, S. Balaz and L. J. Brillson, *Appl. Phys. Lett.*, 2013, **102**, 192910.

42. M. A. Melo, Z. Wu, B. A. Nail, A. T. De Denko, A. F. Nogueira and F. E. Osterloh, *Nano Lett.*, 2018, **18**, 805-810.

43. R. Konta, T. Ishii, H. Kato and A. Kudo, *J. Phys. Chem. B*, 2004, **108**, 8992-8995.

44. S. Nishioka, J. Hyodo, J. J. M. Vequizo, S. Yamashita, H. Kumagai, K. Kimoto, A. Yamakata, Y. Yamazaki and K. Maeda, *ACS Catalysis*, 2018, DOI: 10.1021/acscatal.8b01379, 7190-7200.

45. K. Maeda, K. Teramura, H. Masuda, T. Takata, N. Saito, Y. Inoue and K. Domen, *J. Phys. Chem. B*, 2006, **110**, 13107-13112.

TOC

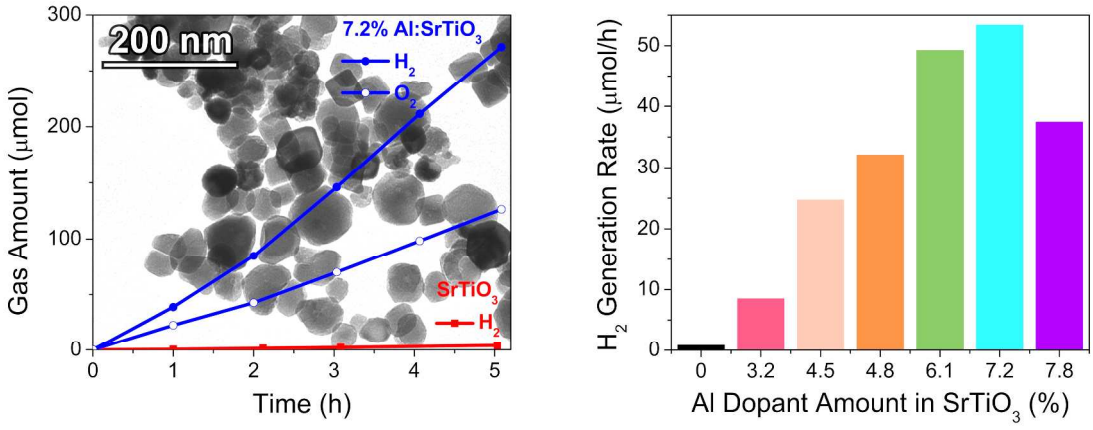

Photovoltage and overall water splitting activity of nanocrystals of aluminium-doped $SrTiO_3$ correlate with aluminum content.